

4D Printing of Shape-Memory Semi-Interpenetrating Polymer Networks Based On Aromatic Heterochain Polymers

Kseniia N. Bardakova,* Bato Ch. Kholkhoev, Ivan A. Farion, Evgenii O. Epifanov, Olga S. Korkunova, Yuri M. Efremov, Nikita V. Minaev, Anna B. Solovieva, Peter S. Timashev, and Vitaliy F. Burdukovskii

Most of the presently known thermosensitive shape-memory polymers suitable for 4D printing have insufficient mechanical strength and thermal stability that restricts their potential areas of application. Here, new photosensitive compositions (PSCs) based on aromatic heterochain polymers – poly-*N,N'*-(*m*-phenylene)isophthalamide (MPA) or poly-2,2'-(*p*-oxydiphenylene)-5,5'-dibenzimidazole (OPBI) – for DLP printing are proposed. Thermal post-curing and supercritical carbon dioxide (scCO₂) are used for post-processing of the structures. During the scCO₂ treatment the removal of unreacted monomeric component (*N,N*-dimethylacrylamide) and its uncrosslinked oligomers is accompanied by the preservation of the initial degree of crosslinking. The more stable shrinkage is observed for the combined post-processing method (T°+scCO₂) in the case of OPBI-PSC and after the heat treatment for MPA-PSC specimens. The method of post-processing and the nature of the heterochain polymer strongly affect the mechanical properties and thermal resistance of the structures. The tensile strength has the maximum value after the thermal post-treatment (101.1 ± 7.1 and 78.4 ± 5.1 MPa of OPBI-PSC and MPA-PSC, respectively). The intense destruction of the materials is observed at 393 and 408 °C for MPA-PSC and OPBI-PSC, respectively. Moreover, the 4D-printed structures exhibit excellent shape memory performance at transition temperatures >100 °C, thus have a great potential for the use in aerospace, robotics, sensorics.

advent of smart materials. These materials are called smart due to their self-sensing, self-adaptability, memory capabilities and manifold functions.^[1,2] Smart materials are capable of transforming their physical properties (dimensions, shape, stiffness, viscosity, adhesion, and color) following the action of different stimuli, namely, temperature, mechanical strength, electric current, light, magnetic field, chemicals, etc.^[3–5]

A combination of smart materials and 3D printing has resulted in a new field known as 4D printing. 4D printed articles may be used in different fields, including electronics,^[2] aerospace industry,^[1,2] engineering,^[6] sensorics,^[2] robotics and medicine.^[7]

Thermosensitive shape-memory polymers (SMPs) are the most widely studied and used group of materials.^[8] In the structure of heat-sensitive SMPs, stiff segments are responsible for the retention of the permanent shape, while flexible segments are responsible for the fixation and retention of the temporary form.^[8] Compared with inorganic ceramics and metallic smart materials, SMPs possess

such advantages as simpler processing, chemical stability, high stress tolerance, and high recoverable strains.^[4]

A significant problem of the wide use of both 4D printing and 3D printing in general is a limited range of polymeric

1. Introduction

New interesting opportunities for the practical application of additive technologies or 3D printing have emerged with the

K. N. Bardakova, E. O. Epifanov, N. V. Minaev, P. S. Timashev
Institute of Photonic Technologies

Research center “Crystallography and Photonics”
Russian Academy of Sciences
2 Pionerskaya st., Troitsk, Moscow 108840, Russia
E-mail: arie5@yandex.ru

K. N. Bardakova, Y. M. Efremov
World-Class Research Center “Digital Biodesign and Personalized
Healthcare”
Sechenov University
8-2 Trubetskaya st., Moscow 119991, Russia

K. N. Bardakova, Y. M. Efremov, P. S. Timashev
Institute for Regenerative Medicine
Sechenov University

8-2 Trubetskaya st., Moscow 119991, Russia

B. Ch. Kholkhoev, I. A. Farion, O. S. Korkunova, V. F. Burdukovskii
Baikal Institute of Nature Management
Siberian Branch of the Russian Academy of Sciences
6 Sakhyanovoy st., Ulan-Ude 670047, Russia

A. B. Solovieva, P. S. Timashev
Semenov Institute of Chemical Physics
Russian Academy of Sciences
4 Kosygina st., Moscow 119991, Russia

P. S. Timashev
Lomonosov Moscow State University
Chemical Department
1–3 Leninskiye Gory, Moscow 119991, Russia

 The ORCID identification number(s) for the author(s) of this article can be found under <https://doi.org/10.1002/admt.202100790>.

DOI: 10.1002/admt.202100790

materials, with the high mechanical strength being a requirement for the manufactured articles;^[9] this is particularly important when parts for the aerospace and structural components industries are designed. For example, in the review,^[10] the authors describe the mechanical characteristics of commercially available polymeric compositions for 3D printing. Most of the materials have the tensile strength in the range of 30–40 MPa and the elongation at break of 5–10%. Polyetheretherketone, “PEEK HP3” have a higher tensile strength (90 MPa). Most of the previously described thermosensitive SMPs (polyurethanes, cross-linked polyethylene, poly- ϵ -caprolactone, polynorbornene, etc.^[11–15]) also have insufficient mechanical characteristics and low shape recovery temperatures (<100 °C). Only a few reports are devoted to high-performance thermosensitive SMPs (polyimides,^[16–19] poly(arylene ether ketones),^[20,21] benzoxazine-epoxy composites^[22]); however, only a small number of them are suitable for the use in 4D printing technologies.^[19,22] For example, X. Li et al. synthesized a polyimide with reactive methacrylate groups for the formation of photocurable inks based on it.^[19] The resulting inks can be used for both digital light processing (DLP) and extrusion molding 4D printing of high-temperature (about 160 °C) shape memory materials. However, these materials have relatively low tensile strength in the range of 30–45 MPa. The new approach for 4D printing of high-performance thermoset based on epoxy resin, benzoxazine and carbon nanotubes was described.^[22] Printed and post-processed composite specimens exhibit high thermal stability (>300 °C) and a good shape memory performance at 190 °C. Nevertheless, the tensile strength of the obtained materials does not exceed 60 MPa. Thus, it can be concluded that 4D printable SMPs with both mechanical strength and high shape recovery temperatures are of considerable interest.

Aromatic polyamides and polybenzimidazoles are important classes of heterochain polymers for engineering. A distinguishing feature of such polymers is the presence of aromatic fragments, as well as amide bonds or benzimidazole cycles in their structure; these fragments provide a rigid chain character to the macromolecules. Besides, their macromolecules interact with each other via hydrogen bonds that results in the formation of dense multilevel intermolecular packing. As a consequence, aromatic polyamides possess prominent mechanical (with Young's modulus ≥ 1 GPa) and thermal (decomposition temperature ≥ 400 °C) characteristics.^[23] Polybenzimidazoles exceed most of the presently known commercially available polymers in the performance characteristics.^[24,25] This makes them attractive for the creation of high-strength and heat-resistant structural materials, including those for the aerospace industry. At the same time, to process polymers of this class into 3D products by traditional methods, high temperatures and pressures are required, due to their high glass transition temperatures (T_g); this leads to a significant energy consumption.

Vat photopolymerization is a group of 3D printing methods based on the selective curing of liquid photosensitive compositions (PSCs) by the action of light, which allows one to form products with complex geometric shapes based on a wide range of different polymers under mild conditions; this is often unreachable, when using traditional methods. At present, the most wide-spread approach to modifying high-performance aromatic heterochain polymers for their use in vat photopoly-

merization is to graft various unsaturated groups (for example, (meth)acrylate and/or maleimide) to the polymer backbone or end groups.^[19,26–29] However, such approaches are laborious and difficult to implement on an industrial scale. Another way is to combine pristine polymers with photosensitive components.^[30–35] As a result of photopolymerization of such systems, semi-interpenetrating polymer networks (SIPN) are formed, which possess a number of attractive properties, including shape-memory performance.^[33]

Recently,^[30,31,35] we have shown that heat-resistant mechanically strong 3D structures can be obtained based on PSCs containing poly-*N,N'*-(*m*-phenylene)isophthalamide (MPA), using laser stereolithography (SLA). However, to the best of our knowledge, no one has ever reported the fabrication of 3D-printed structures based on aromatic polybenzimidazoles through vat photopolymerization. The reason is that most of polybenzimidazoles show a limited solubility in both traditional organic solvents and reactive diluents. Poly-2,2'-(*p*-oxydiphenylene)-5,5'-dibenzimidazole (OPBI) is one of the few representatives of this class of polymers that is readily soluble in aprotic dipolar solvents due to the presence of a bridging ether group.

Another method of vat photopolymerization is DLP, which allows one to form products in a shorter time, since each layer is illuminated by a diode matrix, and not scanned by a laser beam as it is performed in SLA; this is beneficial, when printing large objects with few details. In addition, final DLP products contain a smaller amount of uncured resin in comparison with SLA products, because in DLP there is no difference between the outline and the inner area; in SLA, the laser scanning pattern focuses mostly on the outline of each layer to reduce the building time.^[36]

On the other hand, with the use of DLP, each layer is pixelated, there are shadow areas between pixels, that is the reason for incomplete PSC curing.^[37] This leads to anisotropy of the product properties and their dependence on the direction of assembly.^[10] The best possible mechanical properties of the products are also limited due to the steric hindrances in the solidifying PSC, decelerating the diffusion of radicals formed during irradiation.^[38,39] The incomplete curing leads to insufficient long-term stability of the products and changes in their properties over time.^[40,41] Therefore, it is important to ensure the high conversion of active groups of PSC components by post-curing, or to remove the unreacted PSC from the product.

Among the post-curing methods, the most common ones are the thermal and UV treatment,^[40] ultrasound methods, cleaning in organic solvents, and combinations of these methods are also widely used.^[10,36,42] UV curing results in crosslinking of the unreacted PSC components during printing, and the approach is effective for open-cell sub-micrometer structures. For structures with complex shapes, shape distortions due to nonuniform exposure are reported,^[43] and immersion of the sample in a photoinitiator solution^[38] may be additionally required.

Thermal post-curing is used as an effective and simple method for improving the mechanical properties, increasing T_g and dehydrating the samples.^[44] Due to an increase in the mobility of polymer chains and radicals, which are unreactive at room temperature due to steric hindrances, additional polymerization of the sample occurs under the thermal post-curing

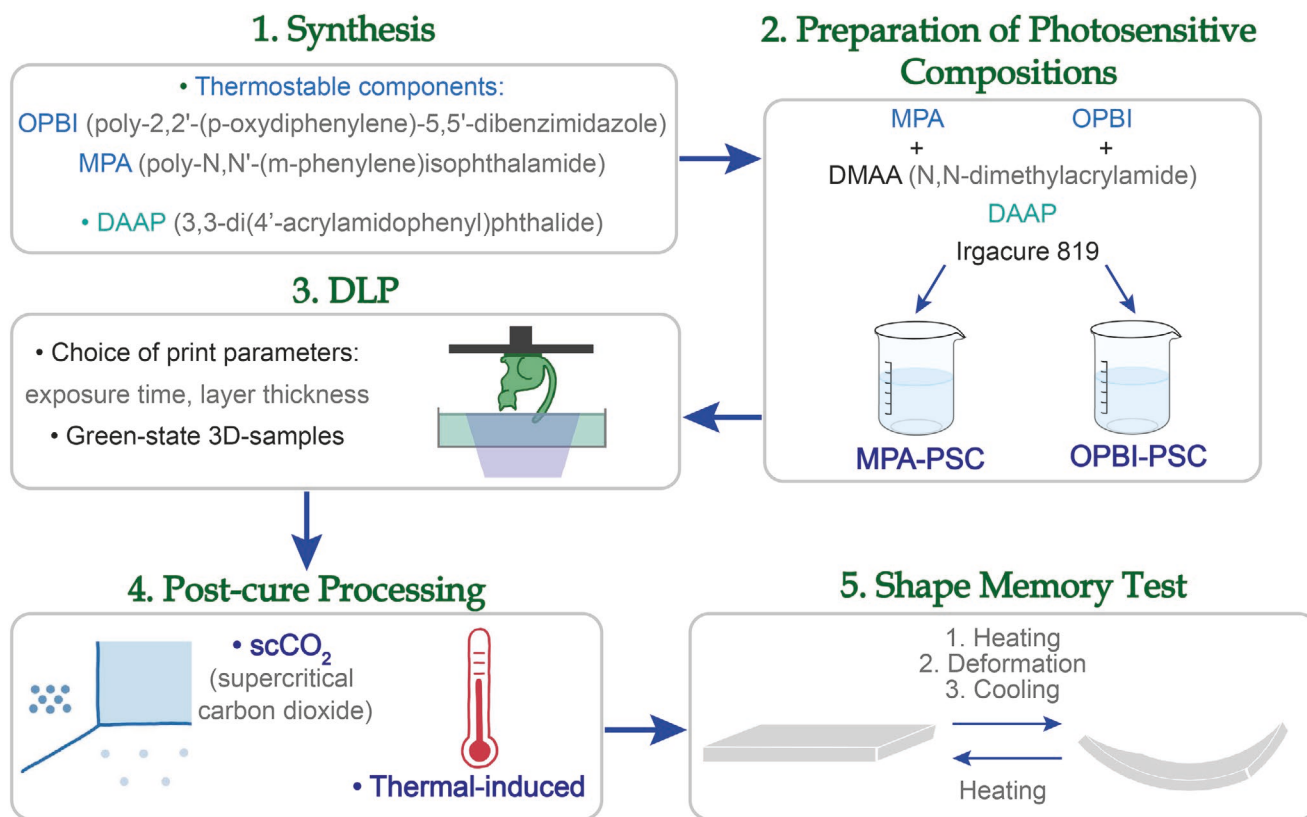


Figure 1. The main stages of the work.

conditions. Since thermal post-curing does not depend on diffusion of the photoinitiator inside the sample, the method is not sensitive to the geometry of the product.^[38] However, thermal post-curing results in higher shrinkage strains than those in UV curing.^[40,45] Therefore, there are more residual stresses in the samples, that can further lead to defects and destruction. Thus, each of the currently known methods of post-processing of 3D printed products has certain disadvantages predetermining the need to develop new approaches.

Supercritical carbon dioxide (scCO_2), which is above its critical pressure and temperature (31.1 °C and 7.38 MPa), is a nontoxic, nonflammable, nonexplosive, inexpensive reagent.^[46–48] scCO_2 has a high diffusion coefficient and low viscosity; this favors mass transfer. It is used for the synthesis and modification of polymers, including impregnation with fillers, sterilization, removal of solvents (so-called “supercritical drying”) and small molecules from polymeric materials (residual UV stabilizers, monomers, and oligomers).^[49,50] Considering the above, the use of scCO_2 is of interest as a “soft” method of post-processing of 3D structures in order to maintain their shape, minimize shrinkage and, therefore, reduce internal stresses in the polymer network.

The main aims of this study were the following

1. For the first time, using the DLP method, to form 3D structures from SIPNs, based on a polybenzimidazole such as OPBI.
2. To evaluate the influence of the nature of a linear hetero-chain polymer (OPBI and MPA) on the process of SIPN

formation by the DLP method, as well as on the mechanical and thermal characteristics of the prepared materials.

3. For the first time, to investigate the possibility of using scCO_2 for post-processing of 3D printed structures, as well as to assess its effect on the properties of materials.
4. To investigate the shape memory effect of the obtained materials.

To achieve the set aims, the work was divided into the corresponding stages (**Figure 1**). Initially, the syntheses of heat-resistant polymers such as MPA and OPBI, as well as of a bifunctional cross-linker such as 3,3-di(4'-acrylamidophenyl)phthalide (DAAP) were carried out. PSCs were obtained by dissolving the synthesized compounds in an active solvent, *N,N*-dimethylacrylamide (DMAA). The resulting PSCs were used to form 3D structures by the DLP method. At the next stage, the formed green-state 3D-samples were post-processed by thermal processing or in the scCO_2 environment. Next, we studied the physical, mechanical, and thermal properties of the 3D-samples, as well as the shape memory effect.

2. Experimental Section

2.1. Materials

Isophthaloyl chloride ($\geq 99\%$, Sigma-Aldrich), *m*-phenylenediamine ($\geq 99\%$, Sigma-Aldrich), 3,3'-diaminobenzidine ($\geq 99\%$,

Sigma-Aldrich), 4,4'-oxy-bis(benzoic acid) (99%, Sigma-Aldrich), acrylic acid (99%, Sigma-Aldrich), DMAA (99%, contains 500 ppm of monomethyl ether hydroquinone as inhibitor, Sigma-Aldrich), methanesulfonic acid ($\geq 99\%$, Sigma-Aldrich), P₂O₅ (99%, Sigma-Aldrich), Irgacure 819 photoinitiator (Ciba Specialty Chemicals, Switzerland) were used without further purification. Anilinephthalein was synthesized from o-phthaloyl chloride and *sym*-diphenylurea (see Figure S1 in the Supporting Information). *N,N*-dimethylformamide (DMF) and *N*-methyl-2-pyrrolidone were distilled over P₂O₅ in vacuo. Acryloyl chloride was obtained by the method described.^[51] Eaton's reagent was prepared by dissolving 3 g of P₂O₅ in 20 mL of methanesulfonic acid at 60 °C with stirring.

2.2. Synthesis of DAAP

DAAP was prepared according to the previously described method.^[30] A three-necked flask equipped with a mechanical stirrer, argon inlet, and outlet was loaded with 0.003 mol of aniline phthalein and 10 mL of *N*-methyl-2-pyrrolidone. The solution was thermostated at a temperature of -20 °C for 10–15 min, after that, 0.006 mol of acryloyl chloride was added. The reaction mixture was stirred for 30 min at this temperature and then for 30 min at 20 °C. After the reaction completion, the product was isolated by precipitation into water, filtered, washed several times with water, and dried in vacuum at 45 °C. The yield was 96%. M.p. is 148.5–150.0 °C. IR spectrum (ν , cm⁻¹): 3273 (N–H), 1658 (amide C=O). ¹H NMR spectrum (δ , ppm): 11.8 (N–H), 5.9, 7.0 (CH₂=CH–), 6.5 (CH₂=CH–), 7.1–7.9 (C_{Ar}–H). ¹³C NMR spectrum (δ , ppm): 169.8 (C=O phthalide), 165.5 (C=O amide), 128.7 (CH₂=CH–), 127.6 (CH₂=CH–), 117.3–118.4, 134.7–154.1 (C_{Ar}). Calculated for C₂₆H₂₀N₂O₄ (%): C, 73.58; H, 4.72; N, 6.60. Found (%): C, 73.33; H, 4.84; N, 6.54.

2.3. Synthesis of MPA and OPBI

MPA was prepared by polycondensation of equimolar amounts of *m*-phenylenediamine and isophthaloyl chloride according to the previously described method.^[30] $\eta_{inh} = 0.99$ dL g⁻¹ (DMF, 20 °C). IR spectrum (ν , cm⁻¹): 3380 (N–H), 1653 (C=O). ¹H NMR spectrum (δ , ppm): 10.5 (N–H), 7.4–8.6 (C_{Ar}–H). Calculated for C₁₄H₁₀N₂O₂ (%): C, 70.59; H, 4.20; N, 11.76. Found (%): C, 69.81; H, 4.58; N, 11.64.

OPBI was prepared by high-temperature polycondensation of 3,3'-diaminobenzidine and 4,4'-oxy-bis(benzoic acid) in Eaton's reagent according to the known methods.^[52] $\eta_{inh} = 2.40$ dL g⁻¹ (DMF, 20 °C). IR spectrum (ν , cm⁻¹): 3070 (N–H), 1662 (C=N), 1444 (C–N), 1237 (C–O). ¹H NMR spectrum (δ , ppm): 13.0 (N–H), 7.3–8.3 (C_{Ar}–H). Calculated for C₂₆H₁₆N₄O (%): C, 78.00; H, 4.00; N, 14.00. Found (%): C, 77.79; H, 4.43; N, 13.94.

2.4. Solubility Test and Preparation of PSCs

To study the solubility of DAAP and the polymers, the calculated weighed portion of the substance was stirred in DMAA using a magnetic stirrer for 24 h at room temperature. To

Table 1. Composition of PSCs.

PSC ^{a)}	DMAA	DAAP	MPA	OPBI	Irgacure 819
MPA-PSC	79	10	10	0	1
OPBI-PSC	79	10	0	10	1

^{a)}The concentration unit of every component is wt%.

obtain PSCs, a polymer (MPA or OPBI) and DAAP were sequentially dissolved in DMAA with magnetic stirring. The Irgacure 819 photoinitiator was added to the resulting homogeneous solution which was further stirred for 24 h until the complete homogenization. The composition of the studied PSCs is shown in Table 1 (see Section 3.1.).

2.5. DLP 3D Printing Process

The formation of 3D structures was carried out using a KLD-LCD1260 modified projection DLP 3D printer (Kelant 3D Printer, China). A UV integrated diode matrix with $\lambda = 405$ nm and the power of 50 W (Chanzon Technology, China) with a constant current driver (the voltage was 32 V, the current was 1500 mA) was used as a radiation source. A standard 5.5-inch 2K LCD screen with a resolution of 1440 × 2560 pixels was used as a gate; the size of each pixel was 47 × 47 μm^2 . A 30 mL vessel made of anodized aluminum with a bottom made of a FEP (Fluorinated Ethylene Propylene) film was used as a reservoir for the PSC.

To select the exposure time of DLP printing, a test matrix model in the form of a 35 × 10 mm² area with a height of 0.2 mm was designed. Areas of 2 × 2 mm² were sequentially illuminated with an exposure time from 5 to 55 s with a step of 5 s. The dependence of the depth of PSC curing on the exposure time was measured at a thickness of the print layer of 50, 100, and 250 μm . The thickness of the photocrosslinked material was measured using a mechanical watch micrometer with an accuracy of 5 μm .

Printing of 3D structures was carried out with the following parameters: the printing step was 50 μm , the exposure time of the first three layers was 60 s, the exposure time of the subsequent layers was 15 s for MPA-PSC and 30 s for OPBI-PSC. After the completion of printing, the 3D structures were additionally irradiated for 1 min with a UV light-emitting diode (with the wavelength of 365 nm and the power of 100 W) (Chanzon Technology, China). To study the mechanical and thermomechanical properties and for the shape memory test of the photo-crosslinked materials, the 3D structures were formed as bars with the dimensions of 30 × 5 × 2 mm³. The data in the Supporting Information contain the source files used to print the complex 3D models, as well as the links to the 3D models downloaded from the thingiverse.com website, which publishes them under a Creative Commons license.

2.6. Post-cure Processing

Green-state samples in the form of bars were divided into three groups. The first group was heated in a muffle furnace to a temperature of 150 °C and kept there for 1 h. The second group was treated for 1 h in the scCO₂ environment at a pressure of

20 MPa and a temperature of 50 °C in a high-pressure reactor. The third group was first kept in a muffle furnace at 150 °C for 1 h, then treated in the scCO₂ environment ($P = 20$ MPa, $T = 50$ °C, 1 h). For each group, the change in the mass and linear dimensions was recorded using a vernier caliper.

2.7. Analytical Methods

2.7.1. Spectroscopic Methods

To assess the absorption indices of the “Irgacure 819” solution (1 wt% in DMAA) and PSCs at the operating wavelength of the projection printer equal to 405 nm, the optical density was measured using a Cary-50 spectrophotometer (Varian Optical Spectroscopy Instruments).

IR spectra were recorded with an Alpha spectrometer (Bruker Optik GmbH) in the wavenumber range of 4000–400 cm⁻¹. The samples were prepared as KBr pellets. NMR spectra of polymers were recorded with a WP-200 SY, 200.13 MHz (Bruker) and a VXR-500S, 500 MHz (Varian) spectrometers. DMSO-d₆ was used as a solvent, tetramethylsilane was the internal standard.

To obtain IR spectra in scCO₂, a Nicolet Impact 410 FTIR spectrophotometer (Melles Griot) equipped with a high-pressure optical cell with an internal volume of about 1 mL, installed in the cuvette compartment of the spectrometer, was used. High-pressure CaF₂ windows with a thickness of 15 mm were installed in the cell body, with a gap of 1 mm between them, which was the working area, in which the absorption spectra were obtained. Samples in the form of bars were placed in the inner volume of the high-pressure reactor, in the area below the optical windows. The measurements were carried out in scCO₂ at the environmental parameters of 20 MPa and 50 °C, after keeping the sample under these conditions for 4 h. To obtain IR spectra of DMAA, 10 µL of the solvent were clamped between the flat surfaces of two round CaF₂ plates with a diameter of 15 mm. Each IR spectrum was calibrated by the intensity of the C–N vibration (1419 cm⁻¹).

2.7.2. Characterization of PSCs

The photorheological experiments were carried out as three parallel in situ measurements with a Physica MCR302 instrument (Anton Paar, Australia). A UV integrated diode matrix, similar to that installed in a DLP 3D printer, was used as a light source with $\lambda = 405$ nm. UV radiation was emitted upward for 30 s through a neutral density filter, reducing the radiation to a level corresponding to that in the DLP 3D printer after the LCD screen. The measurements were carried out using PSCs with a thickness of 500 µm and a diameter of 25 mm at a constant frequency of 10 Hz and an amplitude of 0.01%. The samples were pre-equilibrated for 70 s prior to measurement.

The change in the temperature inside PSCs versus the exposure time of the layer was studied in the following experiment. PSC was poured into a printer bath, an ultrathin thermocouple (K-type, Omega, USA) was placed in it, and the movable platform was lowered to a layer height of 50 µm. For 60 s, the PSC was photocured, the temperature change was recorded using a TPM210 meter (OVEN, Russia).

2.7.3. Characterization of 3D-Printed Samples

The study of the materials' mechanical characteristics was carried out using an Instron 3367 testing machine at a temperature of 20 °C and a relative humidity of about 50% at a stretching rate of 1 mm min⁻¹. For each group of samples at least five specimens were tested and averaged to determine the tensile properties. Bluehill Lite software (USA) was used for statistical analysis. Data were analyzed by Student t-test with significance level p -value less than 0.05. The obtained results were reported as mean \pm standard deviation (SD).

DMA was carried out in the bending mode using a DMA242C analyzer in the temperature range of 25–200 °C at a frequency of 1 Hz, a dynamic force of 5 N and a heating rate of 5 °C min⁻¹.

TGA was conducted with a STA 449 F3 thermal analyzer (Netzsch) at a heating rate of 10 °C min⁻¹. The visualization of changes in 3D structures upon heating was recorded using a video camera. A 3D structure (“Simon’s Cat” of 13 mm high) was placed on an aluminum substrate in the muffle furnace (volume 196 cm³) connected to a TPM210 PID controller (OVEN, Russia). Heating was started at 30 °C and proceeded to 400 °C at a rate of 19 °C min⁻¹. The video was recorded using an XCAM1080PHA camera (ToupTek, China) and a telephoto macro lens, which allowed obtaining an image of a 3D structure inside a muffle furnace. The topography of 3D structures was estimated by SEM with a Phenom Pro X (Phenom-World BV, Netherlands) and a Huvitz HRM (Huvitz, South Korea) 3D microscopes.

2.8. Shape Memory Test

The shape memory of the samples was studied in the bending mode in air. The experiment included the following consecutive stages. At the first stage, the material was heated to the transformation temperature (T_{tran}) and bent under an external load at an angle θ_b . Then the temperature was lowered to 30 °C and held for 15 min to fix the temporary shape. The fixation angle (θ_f) was determined after removing the external load. To restore the shape of the material, the temperature was raised again to T_{tran} , and the angle (θ_f) was fixed at certain time intervals. The shape fixation (R_f) and shape recovery (R) coefficients of 3D printed samples were calculated using the formulas^[53]

$$R_f = (\theta_f / \theta_b) \times 100\% \quad (1)$$

$$R = [(\theta_f - \theta_t) / \theta_f] \times 100\% \quad (2)$$

3. Results and Discussion

3.1. Design of PSCs

For the formation of 3D structures, PSCs were obtained, consisting of a monomer and a bifunctional cross-linker, capable of forming a 3D polymer network as a result of photopolymerization, as well as linear polymers, MPA and OPBI (Figure 2), which improve the thermal and mechanical characteristics of the materials.

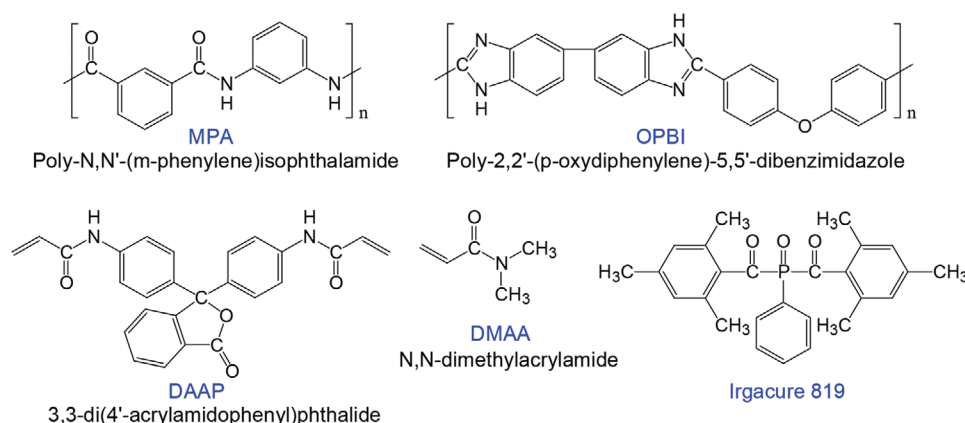


Figure 2. Structures of MPA, OPBI, DAAP, DMAA, and Irgacure 819.

The monomer in PSCs acts also as a solvent, therefore, in addition to the high polymerization rate under UV radiation, it must be a good solvent for both the cross-linker and linear polymers. It is known that MPA and OPBI are soluble in polar organic solvents of the amide type such as DMF and *N,N*-dimethylacetamide.^[23,24] Therefore, to obtain PSCs, such an unsaturated structural analog of these solvents as DMAA was chosen (Figure 2). It was found that both MPA and OPBI were soluble in DMAA up to a rather high concentration of 15 wt%.

An aromatic diacrylamide, DAAP, was used as a cross-linker (Figure 2), since it allows one to form 3D structures with high thermal stability,^[30,31] and the presence of the cardo phthalide group gives it good solubility in amide solvents. It has been found that the maximum achievable concentration of DAAP in DMAA is 20 wt%. However, it should be noted that the solubility of the PSC components changes significantly, when they are dissolved together. The study of various ratios of the components allowed us to select the compositions of PSCs (Table 1), which remained stable for a long time (up to 1 year).

The structures of all the PSC components are shown in Figure 2.

3.2. DLP-Based 3D Printing

In this work, we considered two types of PSCs, the composition of which differed in the type of a linear heat-resistant polymer, OPBI, or MPA. As a result of 3D printing, the 3D polymer network was formed from DMAA and DAAP. Since linear thermostable polymers do not contain reactive groups, they are noncovalently incorporated into the formed 3D network, that is, SIPN is formed (OPBI-SIPN and MPA-SIPN). The chemical structure of the linear thermostable polymer can have a significant effect on the parameters of photocuring, namely, on the photocrosslinking kinetics, curing profile, crosslinking density, etc.

3.2.1. Evaluation of Photocuring Behavior of PSCs

It can be seen from the results of the in situ photorheological studies of PSCs (Figure 3) that networks with a slightly higher

plateau modulus ($G' \approx 2.3 \times 10^7$ Pa) were formed in the case of MPA-PSC than they were in the case of OPBI-PSC ($G' \approx 1.9 \times 10^7$ Pa). Moreover, during the photocuring process, the MPA-PSC plateau modulus is achieved sooner than it takes place in the case of OPBI-PSC.

As seen from the absorption spectra (Figure 4), the presence of OPBI in PSC leads to a greater attenuation of the light intensity depending on the depth compared to MPA and Irgacure 819. A D_p coefficient (the depth at which the penetrating light intensity falls to $1/e$ of the surface intensity^[54]) is 103 μm for OPBI-PSC and 319 μm for MPA-PSC. That is, at the initial time at a depth of 50 μm (thickness of the print layer), the 405 nm light intensity is attenuated by $\approx 38\%$ for OPBI-PSC, and by $\approx 14\%$ for MPA-PSC. Thus, OPBI acts as a light absorbing additive or photoblocker, which has a significant effect on the photocrosslinking kinetics and the curing profile.

In addition, during photopolymerization, the opening of C=C bonds is an exothermic reaction and the presence of a photoblocker leads to a smaller temperature jump in the PSC. OPBI is chemically inert, but it absorbs and dissipates energy, and the temperature in OPBI-PSC does not rise as much as it does in the case of MPA-PSC; the maximum temperature increase for OPBI-PSC is about 1.1 $^\circ\text{C}$, and for MPA-PSC it is about

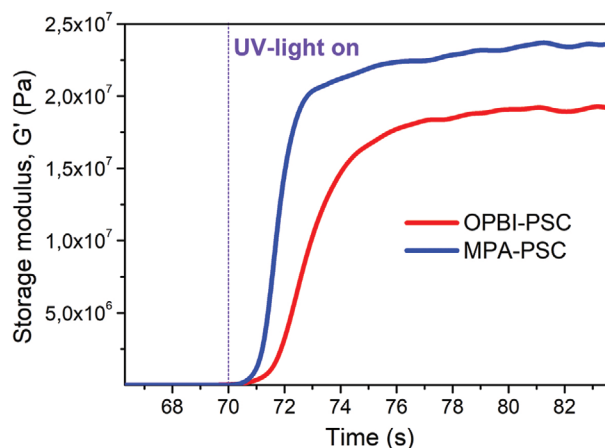


Figure 3. The storage modulus (G') versus time plot from the photorheological experiments.

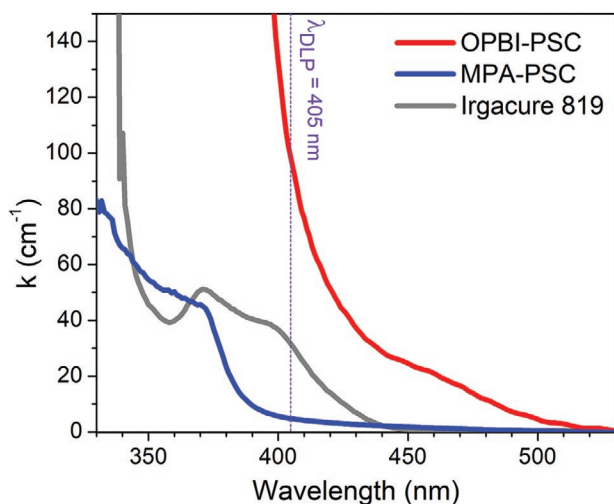


Figure 4. Absorption spectra of OPBI-PSC and MPA-PSC without the photoinitiator; absorption spectrum of Irgacure 819 (1 wt%) in DMAA. At 405 nm, the attenuation coefficients k are: 97.3 cm^{-1} for OPBI-PSC without the photoinitiator, 4.7 cm^{-1} for MPA-PSC without the photoinitiator, 31.3 cm^{-1} for Irgacure 819.

$2.2 \text{ }^\circ\text{C}$ (Figure 5). Note that regulating the temperature change of PSCs by adding photoblockers is relevant, for example, to dental PSCs, where the thermal damage to the pulp and tooth-supporting tissue^[55] is undesirable, or to 3D biomaterial scaffolds that contain cells, proteins, antimicrobial agents.^[56]

It is known that a certain value of critical energy is required to initiate photopolymerization. The parameter of “critical energy to initiate polymerization” is included in the well-known Jacobs’ basic working curve equation; it is often determined in printing using specific PSCs, and mathematical models of the photopolymerization process are built. At the same time, in practice, for the initial selection of parameters, one can limit oneself to measuring the optical absorption of PSCs (Figure 4), that is, to determine the D_p coefficient. By measuring the temperature dependence on the exposure time, one can determine the boundary values of the exposure dose. Therefore, from Figure 5, the maxima of the curves can be taken as the times corresponding to the end of a PSC layer photocrosslinking; this

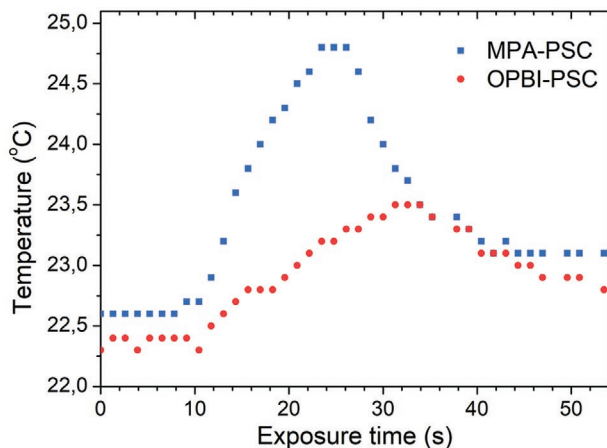


Figure 5. PSCs temperature versus layer exposure time.

time is 23 s for MPA-PSC and 31 s for OPBI-PSC. The ratio of the slopes of the tangent lines to these curves at the start of photocrosslinking shows that, at the initial moment, photocrosslinking of MPA-PSC occurs 2.8 times faster than that of OPBI-PSC. In fact, this numerical value is close to the ratio of the D_p coefficients for PSCs (about 3).

Photopolymerization is a nonlinear process, resulting in that the initial PSC undergoes a complex spatial-temporal change, which can also be traced by the changes in the temperature curves. For a MPA-PSC exposure from 9 to 14 s, an almost linear temperature rise is observed, corresponding to the so-called photoinvariant polymerization, in which the attenuation coefficients are constant, or, in other words, the optical attenuation of the polymerized medium is not different from the pure monomer.^[57,58] One can speak about constant frontal kinetics in the case of MPA-PSC at this stage, because the transmission does not change. Further, after the 14 s of MPA-PSC exposure, a sharp change in the rate of temperature rise is observed, which can be explained by a decrease in the absorption capacity of PSC with increasing the exposure time, due to the continuing process of photodegradation of the photoinitiator.^[54,59] Due to this phenomenon, the light penetrates deeper (D_p increases), the slope of the temperature curve changes. It should be noted that the photocrosslinked material has a lower absorption coefficient compared to uncured PSC.

It is interesting to note the stepped nature of the temperature curve in the case of OPBI-PSC (Figure 5). In this case, we can say that the absorption capacity of PSC does not depend on the exposure time of the layer and is mainly determined by the presence of OPBI in the composition, since the heterocyclic OPBI fragments partially absorb UV radiation. The steps seem to be caused by the inhomogeneity of the monomer-to-polymer conversion profile and optical attenuation (a change in the local transmission due to photobleaching of the photoinitiator and formation of the polymer network).

3.2.2. Determination of Photocuring Modes for MPA-PSC and OPBI-PSC

To establish the exposure time during DLP 3D printing, a test matrix model was designed (Figure 6a), based on which, preset structures were formed using MPA-PSC (Figure 6b) and OPBI-PSC (Figure 6c). The measured plots of the cure depth of PSCs versus the exposure time for printing layers of 50, 100, and 250 μm are shown in Figure 6d,e.

In the case of MPA-PSC, it was possible to form complete layers with a thickness of 50 and 100 μm with exposure times of 15–20 s. In contrast, OPBI-PSC required a two times longer exposure time for the same depths of cure. For a layer with a thickness of 250 μm , it was possible to form elements in the form of cubes only for MPA-PSC. The cube elements made of OPBI-PSC for a layer with a thickness of 250 μm were also crosslinked, but moved away from the substrate due to insufficient adhesion to it. It was possible to measure the curing depth of OPBI-PSC only with the exposure time of >50 s.

One of this study objectives was to assess the effect of the chemical structure of the thermostable polymer (OPBI and MPA) on the mechanical and thermal characteristics of 3D

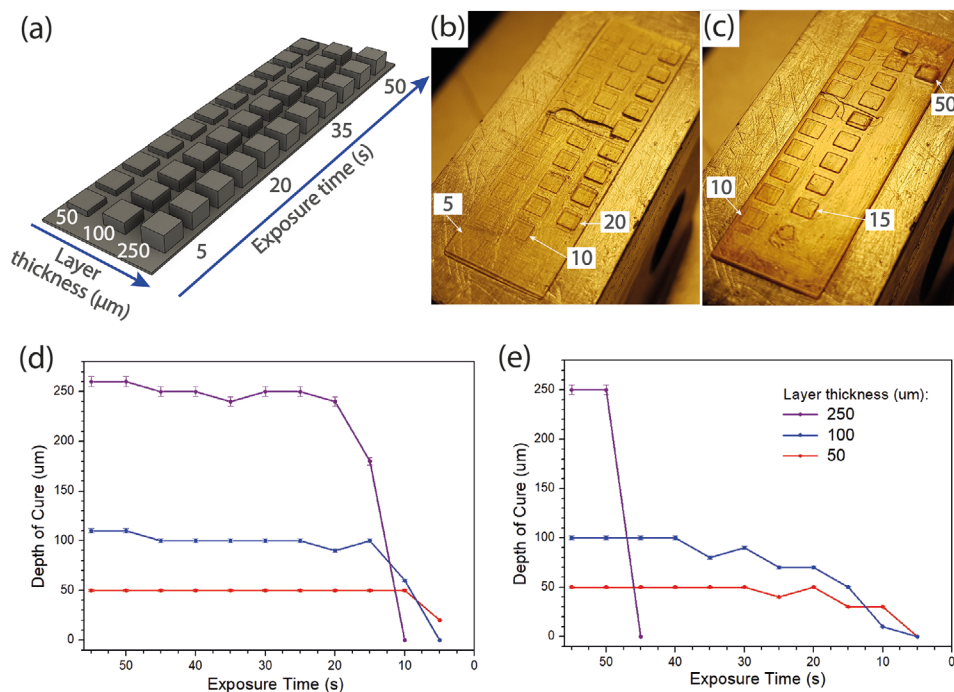


Figure 6. a) A test matrix model, b) structures based on the model formed from MPA-PSC, and c) OPBI-PSC. In panels (b) and (c), for each layer thickness, the minimum exposure time (s), at which the cube element was attached to the platform, is indicated. Plots of the cure depth versus the exposure time for d) MPA-PSC and e) OPBI-PSC for printing layers of 50, 100, and 250 μm .

printed samples. Therefore, the parameters of DLP printing were chosen in such a way as not to take them into account in the future, when characterizing 3D structures. For both PSCs, a layer thickness of 50 μm was recorded. The exposure time of the layer was 30 s for OPBI-PSC and 15 s for MPA-PSC.

3.2.3. Specifics of the Formation of 3D Printed Structures

Using a photoblocker, such as a naphthol-based dye, in a PSC, it is possible to adjust the vertical print resolution,^[9,60] that allows printing complex 3D structures, for example, structures that contain internal channels or high-resolution projections. It is known that, in the methods of vat photopolymerization (for example, SLA and DLP), it is necessary that the light during the polymerization of a layer would reach the previously printed layer, when the subsequent layer is added to the previous one. This ensures that the layers are glued together. However, if the structure under formation is to contain internal channels or high-resolution overhangs, then, when using a deeply transmissive PSC, the channel occlusion (e.g., “bleedthrough”)^[61] or overpolymerization in the Z-direction occurs.^[60] On the other hand, the use of such PSCs allows the 3D model to be split into fewer layers; therefore, the printing speed increases, which is an advantage when forming large objects.

It should be kept in mind, though, that the presence of a photoblocker in a PSC may turn overpolymerization from the Z- to the Y-direction, since there will be different PSC cure profiles (Figure 7a). In the case of MPA-PSC, the light penetrates deeply, and the curing profile is elongated. Hence, the greatest deviation from the dimensions of the computer model will

be along the Z-axis (Figure 7b). In the case of OPBI-PSC, the light penetration depth is less, and free radicals are localized on the surface of the PSC, resulting in a tightly crosslinked, thin curing profile. However, OPBI molecules scatter UV radiation, and heterocyclic OPBI fragments partially absorb it, which leads to broadening of the photocrosslinking area, that is, the geometry of the layer. Therefore, the geometry of the final 3D structure does not correspond to the original model to a greater extent than it happens in the Y-direction. Additionally, the structure has a pronounced 3D relief (Figure 7d,e). While in the case of MPA-PSC (Figure 7c) the projections’ height does not exceed 3–4 μm , then for the OPBI-PSC samples the projections’ height is about 25 μm .

The assessment of the cure profile and topography of the resulting structures allows one to foresee the limitations of a specific PSC for DLP. For both PSCs, in general, it is possible to print structures of complex geometry (Figure 8). However, in the case of OPBI-PSC, distortions are observed when forming models with high-resolution ledges. For example, in Figure S2 (Supporting Information), the nose of the bust is slightly deformed compared to the model.

The composition and physicochemical properties of a PSC, the specifics of PSC photocrosslinking (curing profile, crosslink density, and selected printing parameters) will further influence the shrinkage of the 3D structure during post-processing.

3.3. Post-processing of 3D-Printed Green-State Samples

Due to the physical characteristics of PSCs (viscosity, fluidity), the nature of the components (cationic or radical photoinitiator,

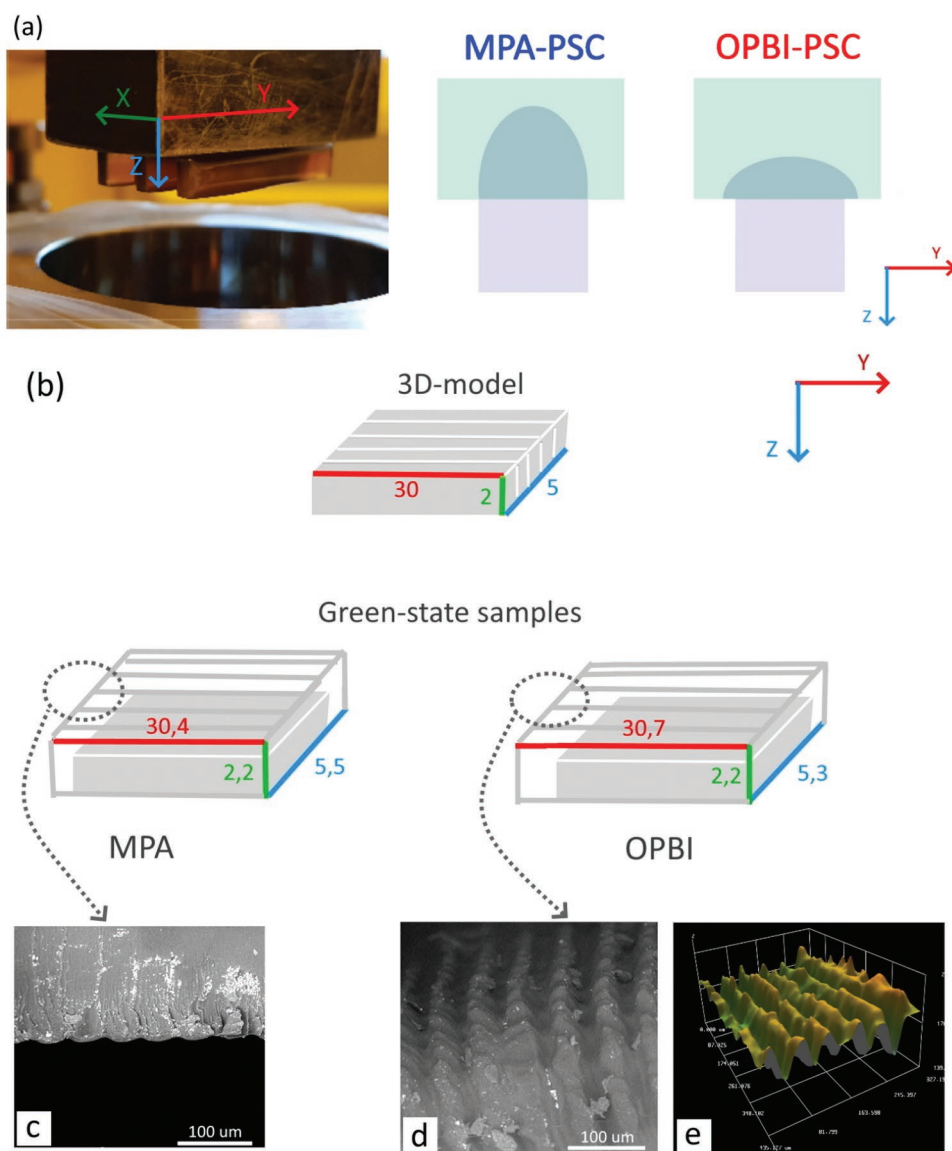


Figure 7. a) Schematic representation of PSC cure profiles and green-state samples as blocks. b) Specified and derived block sizes from MPA-PSC and OPBI-PSC; Insets: SEM green-state samples from c) MPA-PSC and d) OPBI-PSC, respectively, e) 3D microscopy of green-state sample from OPBI-PSC.

the affinity of the components to each other, etc.), limitations of the vat photopolymerization method (for example, the presence of shadow areas for DLP), some PSC remains uncrosslinked in the 3D structures PSC. The presence of uncrosslinked PSC leads to anisotropy of the product properties, and the subsequent post-processing to remove it leads to volumetric shrinkage. In turn, the volumetric shrinkage increases internal stresses in the sample, which can then lead to its deformation and destruction.^[62] Thus, when choosing a post-processing technique, it is necessary to take into account not only the completeness of the uncrosslinked PSC's conversion, but also potential reduction of the volumetric shrinkage of products.

In this work, we used several post-processing methods for green-state samples, which had a different effect on the structures being formed. DMF is a conventional organic solvent in which all of the PSCs' starting materials exhibit good

solubility. Using it for extraction led to the largest weight reduction (12.3% and 8.1%, for OPBI-PSC and MPA-PSC, respectively), while after the scCO₂ and heat treatments, the weight loss was less pronounced (Table 2) (with a slightly higher weight loss after the thermal exposure than that after the scCO₂ treatment).

Note also that, regardless of the post-processing method chosen for the OPBI-PSC group of samples, the weight loss is greater compared to that for the MPA-PSC samples. This can be explained by the fact that, in the case of OPBI-PSC, the polymerization depth is lower due to scattering and partial absorption of UV radiation by the heterocyclic OPBI fragments. As a consequence, green-state samples based on OPBI-PSC contain more of the uncrosslinked PSC. In addition, in this case, a less dense polymer network appears to form, from which the unreacted substances are more easily removed during post-processing.



Figure 8. Examples of 3D structures fabricated from a) OPBI-PSC and b) MPA-PSC by DLP 3D printing. Scale bar is 5 mm.

IR spectroscopy was used to identify the substances extracted during the $scCO_2$ treatment. It was shown that the IR spectra of the extracts (Figure S3, Supporting Information) had the same pattern and contained absorption bands typical for the monomeric component, DMAA, at 1664 cm^{-1} (stretching vibrations of the C=O bonds (Amide I)), 1419 and 1265 cm^{-1} (stretching and deformational vibrations of the C–N bonds) and 1621 cm^{-1} (stretching vibrations of the C=C bonds). However, it should be noted that the intensity of the C=O band in the IR spectra of the extracts is significantly higher in comparison with the intensities of the C=C and C–N bands. During photopolymerization of DMAA, the C=C bonds are opened, resulting in weakening of their conjugation with the C=O bond, which ultimately leads to the increase in the carbonyl group band intensity. During the $scCO_2$ treatment, in addition to monomeric DMAA, DMAA-derived uncrosslinked oligomers formed upon the UV irradiation are also removed. This assumption is further supported by the fact that DAAP, MPA, and OPBI are insoluble in $scCO_2$.

During the heat treatment of green-state samples, the above-mentioned oligomeric products based on DMAA appear to

Table 2. Reduction of green-state samples' mass after post-processing by various techniques.

Sample	DMF	$scCO_2$	T°
OPBI-PSC	12.3%	5.0%	7.2%
MPA-PSC	8.1%	2.3%	4.3%

undergo additional curing, resulting in the increased density of 3D polymer networks cross-linking. The more significant decrease in weight in this case seems to be due to the fact that, along with evaporation of unreacted monomeric DMAA, the moisture is removed and maybe absorbed by linear polymers (OPBI, MPA) which have the groups capable of forming hydrogen bonds.^[23,24]

The greatest weight loss during the DMF extraction is associated with the removal of not only uncrosslinked PSCs components, but also linear polymers (OPBI, MPA). It should also be noted that the extraction of DMF is accompanied by swelling of the samples by 13% in the case of MPA-PSC and by 21% in the case of OPBI-PSC. Thus, the post-processing with the use of DMF leads to the SIPN destruction and disruption of the 3D structure's integrity. This fact also explains the formation of a less dense polymer network for OPBI-PSC in comparison with MPA-PSC.

The shrinkage of the samples was calculated as a ratio of their linear dimensions (length, height, width) after the processing to the dimensions of the green-state samples. For samples from both OPBI-PSC and MPA-PSC after the post-processing, the same tendency is observed: the length increases, the width and height decrease (Figure 9). The shrinkage in width for OPBI-PSC samples is generally more pronounced after the heat treatment (when the crosslinking density of the polymer network increases) than after the removal of the unreacted PSC components with $scCO_2$. This fact can indirectly be confirmed by the curing profile (Figure 7a) showing that the least crosslinked

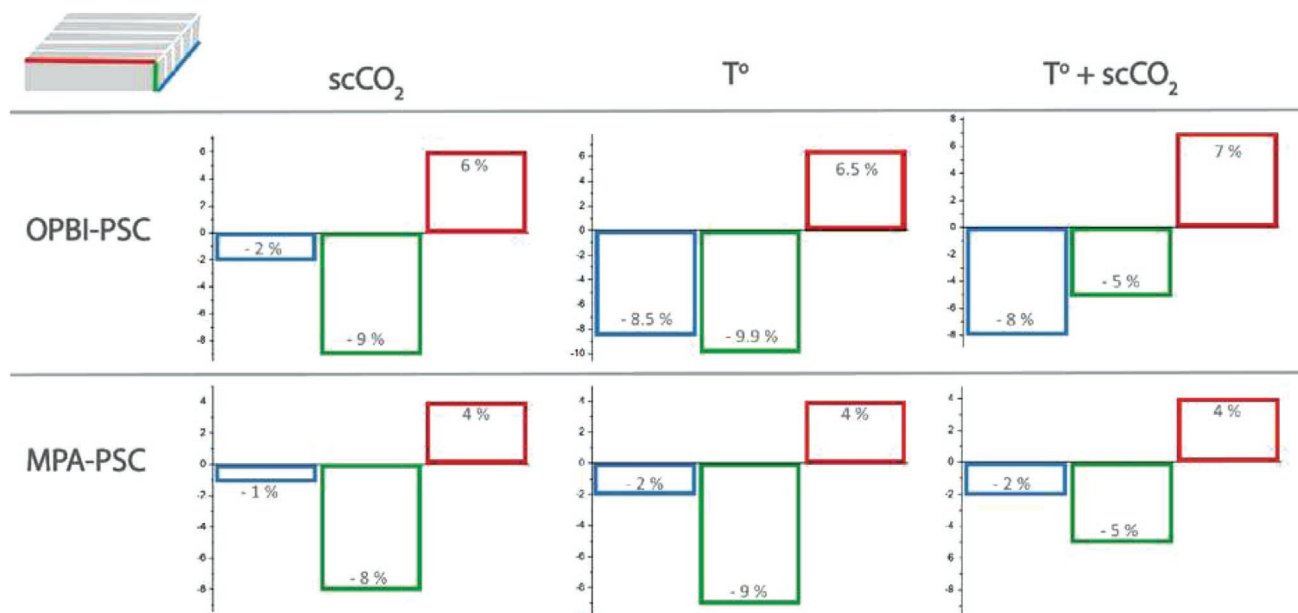


Figure 9. Change in the linear dimensions of green state samples after the scCO₂ post-processing and thermosetting.

areas of the layer are the farthest ones from the diode matrix, that is, the greatest shrinkage occurs in the Z-direction or for the stratified surface. The DLP-printed surface also shrinks due to overpolymerization in the Y-direction. For MPA-PSC, due to overpolymerization in the Z-direction, the layers are more glued together, hence, the shrinkage in width (blue bars in Figure 9) is less pronounced than that for OPBI-PSC.

Additionally, to characterize the shrinkage of the samples, the shrinkage anisotropy coefficient was calculated, which is essentially the ratio of shrinkage rates in the different directions (M_1 , M_2 , M_3), as well as the comprehensive shrinkage stability coefficient (C_s) (Figure 10).^[63]

It follows from the shown relations that the M_2 coefficient determines the DLP-printing surface, while M_1 and M_3 control the stratified surface. Consequently, for heat- or scCO₂-treated OPBI-PSC the shrinkage of the DLP-printing surface will predominate over that of the stratified surface (the M_2 coefficient in these cases is the smallest). For the combined post-processing method (T° + scCO₂), in the case of OPBI-PSC, the more stable shrinkage is observed (the lowest value of the C_s coefficient is 0.26). For a subgroup of MPA-PSC specimens, the structures after the heat treatment are characterized by the highest shrinkage stability. However, it is necessary to mention the strong shrinkage anisotropy for the MPA-PSC samples compared to the OPBI-PSC samples, especially after the exposure to scCO₂.

Thus, the formation of SIPNs, as well as the changes occurring in them as a result of post-processing of green-state samples, are illustrated in Figure 11. DMAA photopolymerization leads to formation of linear macromolecules, while crosslinking is provided via its copolymerization with DAAP. The linear heat-resistant polymer components – MPA and OPBI – fill the formed cellular polymer structure as a peculiar kind of a reinforcing additive. In green-state samples, the non-crosslinked component of PSCs is generally DMAA. When

treating DMF together with DMAA and DMAA-based oligomers formed under UV irradiation, the linear heat-resistant polymers are partially removed. The extraction with DMF leads to the swelling of the samples, i.e., the formed SIPN is partially destroyed. In contrast, during the scCO₂ treatment, DMAA and DMAA-based oligomers are removed insignificantly, and the degree of crosslinking does not change. The thermal post-processing increases the crosslinking density of 3D polymer networks, and DMAA together with the absorbed moisture evaporate.

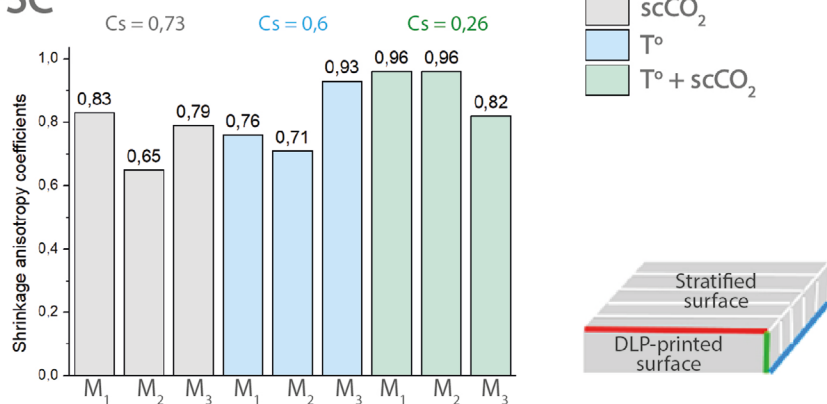
It should be noted that the main drawbacks of the scCO₂ treatment are (i) a limited polarizability ($26.5 \times 10^{-25} \text{ cm}^3$) of carbon dioxide (this means that polar compounds are poorly soluble in this solvent and the addition of cosolvents and modifiers need to be used) and (ii) the need for careful selection and control of operating conditions, such as temperature, CO₂-concentration, depressurization rate, viscosity,^[64] because scCO₂ can act as a foaming agent, especially for glassy polymers.

3.4. Mechanical and Thermal Properties of 3D-Printed Samples

Among the factors that have the strongest effect on the mechanical properties of 3D-printed products, one can highlight the chemical structure of polymers, the free volume, the order in the molecular packing, the polymer network uniformity, the presence of a plasticizer, etc.^[65] The results of our studies on the mechanical properties of green-state and post-processed SIPN are presented in Figure 12 and Figure S4 and Table S1 (Supporting Information).

The higher values of the tensile strength and elongation at break for all of the OPBI-SIPN samples in comparison with the MPA-SIPN samples are noteworthy. This fact may be explained by the nature of the linear heat-resistant polymer: the film based on pure OPBI has a higher tensile strength and is more elastic

OPBI-PSC



MPA-PSC

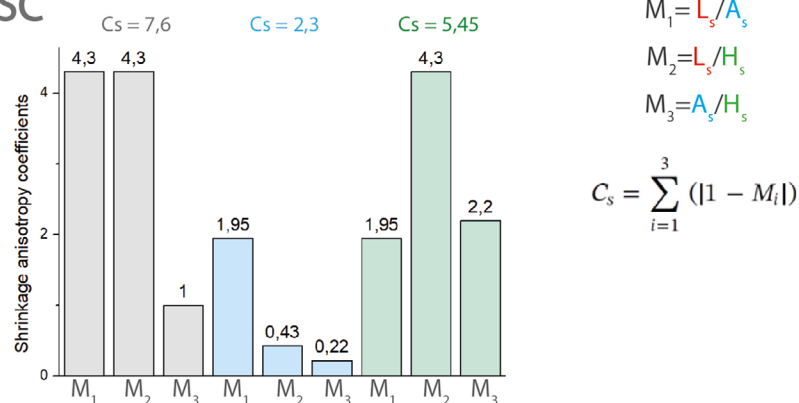


Figure 10. The shrinkage anisotropy coefficients (M_1 , M_2 , M_3) and the comprehensive shrinkage stability coefficient (C_s).

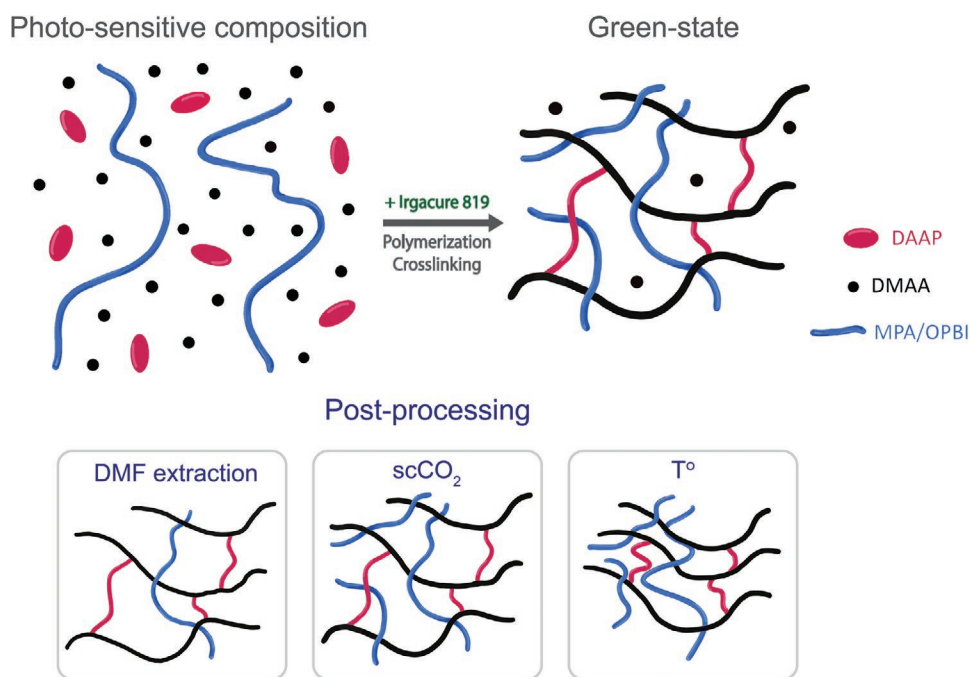


Figure 11. The scheme of a SIPN formation as a result of DLP 3D printing and an illustration of changes in SIPN resulting from post-processing of green-state samples by various methods.

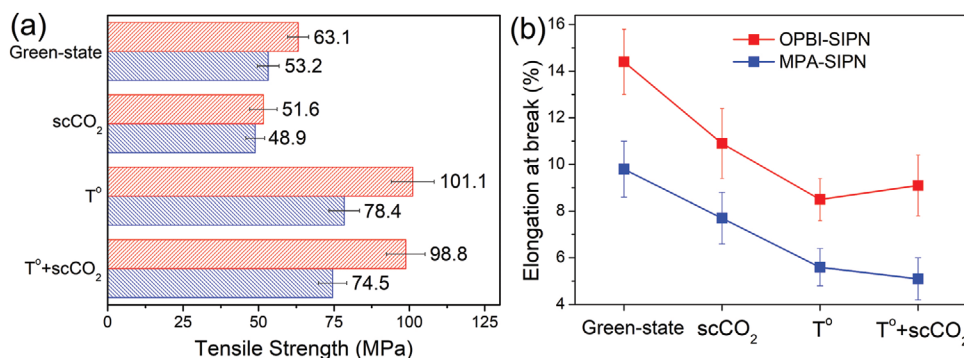


Figure 12. Summary of mechanical properties (a) tensile strength and (b) elongation at break) of OPBI-SIPN and MPA-SIPN post-processed by different methods. Data are represented as the mean \pm SD ($n = 5$, $p < 0.05$).

(Table S1, Supporting Information) compared to the film based on pristine MPA. This is due to a higher molecular weight of OPBI and the presence of the bridging ether group providing the elasticity to the polymer chain. In addition, the greater elongation at break of the green-state samples based on OPBI-SIPN may be explained by the presence of a larger amount of unreacted DMAA, which acts as a plasticizer.

During the scCO₂ treatment, as shown earlier, the removal of DMAA and DMAA-based oligomers is accompanied by the preservation of the initial degree of crosslinking. For these reasons, a slight decrease in the elongation at break of the materials is observed. However, it should be noted that, in the case of OPBI-SIPN, a more significant decrease in the tensile strength occurs than that in the case of MPA-SIPN. This finding appears to be related to the presence of a larger amount of DMAA in green-state samples that is further removed in scCO₂; this leads to large internal stresses. Besides, the scCO₂ post-processing method does not change the number of cross-links in the samples, hence, the tensile strength is comparable to that of green-state samples.

Figure 12 also shows that the tensile strength has the maximum value after the thermal post-treatment for both SIPN. In particular, the increase in the tensile strength in comparison with the green-state OPBI-SIPN samples is 60%, and

for MPA-SIPN, it is 47%. During the heat treatment, a PSC is additionally crosslinked, that is, a more densely cross-linked polymer network is formed, and the mobility of a polymer chain decreases, so T_g increases, and the material rigidity increases, as well. The presented data also show that, after the heat treatment, in both cases the elongation at break decreases by more than 40%. As previously shown, the heat-treated specimens exhibit a significant shrinkage, especially the OPBI-SIPN specimens. Consequently, there are more internal stresses in the samples, and their brittleness is higher. The post-treatment with scCO₂ does not change the SIPN mechanical characteristics.

The summation of the presented data allows us to conclude that the SIPN 3D-printed materials obtained by the DLP method based on MPA and OPBI surpass the mechanical characteristics of most of commercially available materials for 3D printing, which have the tensile strength in the range of 30–40 Mpa.^[10] Using various post-processing methods, it is possible to control the volume of the shrinkage of a formed structure and, as a consequence, its mechanical characteristics.

All the subsequent studies were carried out with 3D-printed samples, which were subjected to the thermal post-processing.

The thermal characteristics of the SIPN were investigated by the TGA method, and the results are shown on **Figure 13** and in **Table 3**.

According to the TGA data (Figure 13 and Table 3), our SIPNs have excellent thermal stability, that is, the intense destruction (a 10% weight loss) of the materials is observed at temperatures above 390 °C. It should be noted, however, that MPA and OPBI have higher thermal stability (Figure S5, Supporting Information, Table 3), and $T_{10\%}$ of the photocurable DAAP-DMAA composition is 358 °C, which is lower than that of the SIPN. In addition, the temperatures of the 2%, 5%, 10%, and 50%

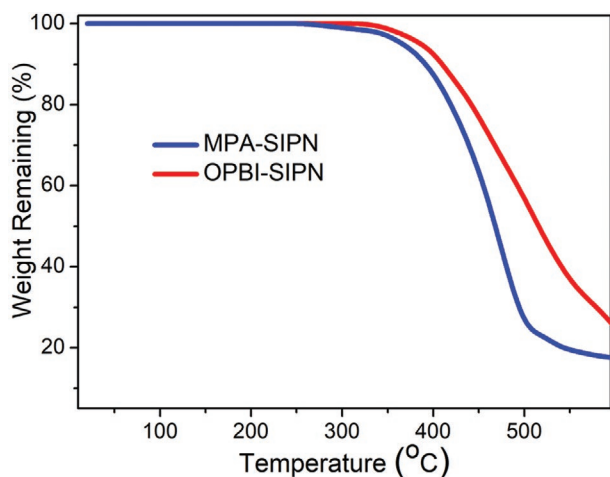


Figure 13. TGA curves of SIPN.

Table 3. Thermal properties of SIPN.

Sample	$T_{29\%}$, °C	$T_{5\%}$, °C	$T_{10\%}$, °C	$T_{50\%}$, °C
MPA-SIPN	340	364	393	472
OPBI-SIPN	360	377	408	516
MPA	384	412	423	603
OPBI	423	476	507	680

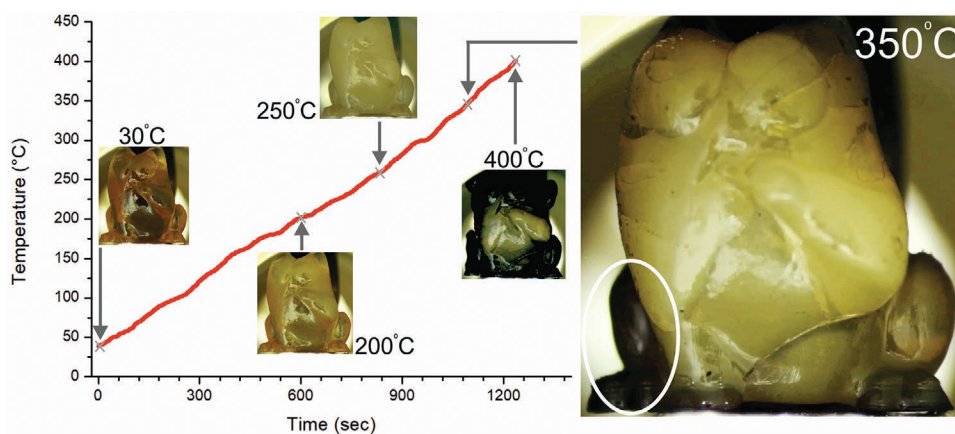


Figure 14. Heating-induced changes in the appearance of an MPA-PSC-based 3D printed structure of “Simon’s cat.” The inset on the right shows an area of the structure that has begun to undergo thermal degradation.

weight loss are higher for OPBI-SIPN compared to MPA-SIPN. The results obtained indicate that the thermal resistance of the linear polymer (MPA and OPBI) influences the thermal resistance of the SIPN. However, this influence is not significant enough, and is largely determined by the thermal resistance of the 3D network (based on DAAP and DMAA) containing the less heat-resistant aliphatic fragments.

The visual changes in an MPA-SIPN-based 3D structure (“Simon’s Cat”) during thermal tests are also shown in **Figure 14**. When increasing the temperature, the structure changes its color and transparency at about 250 °C, then, at about 350 °C, darkening of individual parts, closest to the heating surface, is observed. At about 400 °C, the active destruction occurs, accompanied by darkening of the most of the structure. The obtained results are in a good agreement with the previously conducted TGA indicating that destruction begins at 340 °C, and the intense destruction accompanied by a 10% weight loss occurs at 393 °C (Figure 13 and Table 3). It should also be noted that the structure retains its original shape up to the temperature corresponding to the onset of thermal destruction.

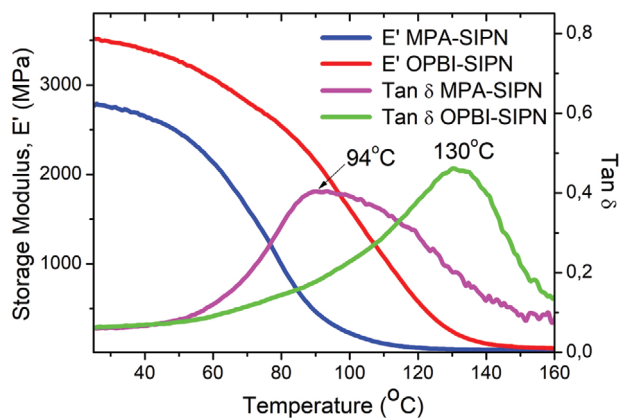


Figure 15. Temperature dependence of the storage modulus and $\text{Tan } \delta$ of SIPN.

3.5. Shape Memory Performance of 3D-Printed Samples

Generally, thermosensitive SMPs contain two phases with different functions. One can melt or soften above the transition temperature (T_{tran}), acting as a “switch.” Another, more thermally stable phase acts as a “fixed point,” providing the necessary strength to fix the temporal shape and restore it. Earlier, a number of works described SIPNs of different compositions with good shape recovery ($R_r > 95\%$).^[33,66] Our SIPNs contain flexible aliphatic fragments formed during DMAA polymerization, rigid crosslinks formed by DAAP, as well as macromolecules of heat-resistant MPA or OPBI. All of this serves as a basis for the study of the shape-memory properties of MPA-SIPN and OPBI-SIPN.

The T_{tran} of SMPs is directly related to the glass transition temperature (T_g). In this regard, SIPNs have been investigated using the DMA method. As seen from **Figure 15** and **Table 4**, the T_g s of MPA-SIPN and OPBI-SIPN are 94 and 130 °C, respectively. The presence of only one broad peak on the tangent δ versus the temperature plots of the investigated materials is characteristic of SIPN.^[34,66] In the case of MPA-SIPN, there are likely submicron regions of differing composition, as indicated by the broader peak in the $\text{Tan } \delta$ plot. Since the original PSCs have the same mass composition and differ only in the type of a linear polymer (MPA or OPBI), then, according to the Fox equation,^[34] the T_g of SIPN would be determined by the glass transition temperature of the linear polymer. T_g of MPA is 271 °C and that of OPBI is 348 °C, hence, OPBI-SIPN has a higher glass transition temperature than that of MPA-SIPN.

Table 4 also shows that in both cases there is a significant difference between the glassy (E_g) and rubbery moduli (E_r), which is one of the criteria of shape-memory polymers, since

Table 4. Thermomechanical properties of SIPN.

Sample	T_g , °C	E_g , MPa ^{a)}	E_r , MPa ^{b)}
MPA-SIPN	94	2778.62	63.86
OPBI-SIPN	130	3518.32	58.82

^{a)} E' at 25 °C; ^{b)} E' at $T_g + 25$ °C.

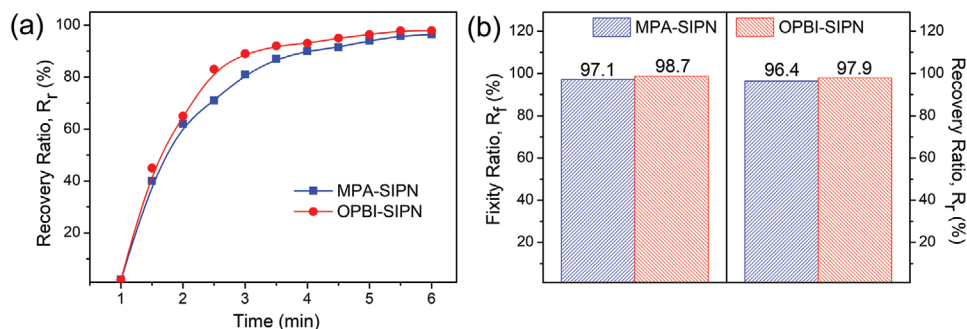


Figure 16. a) R_r versus time for SIPN at $T_{\text{tran}} = T_g + 25$ °C. b) R_f and R_r of SIPN at $T_{\text{tran}} = T_g + 25$ °C.

the shape memory effect is often described by the following mathematical models:^[66]

$$R_f = 1 - E_r/E_g \quad (3)$$

$$R_r = 1 - f_{IR} / \left[(1 - E_r/E_g) f_\alpha \right] \quad (4)$$

where R_f is the shape fixity ratio, R_r is the shape recovery ratio, E_g is the glassy modulus, E_r is the rubbery modulus, f_{IR} is the viscous flow strain and f_α is the strain when $t \gg t_r$.

A high elasticity ratio (E_g/E_r) allows for easy shaping at $T > T_{\text{tran}}$ and a good resistance to the deformation at $T \ll T_{\text{tran}}$.

The results of the shape-memory effect studies of our SIPN are presented in Figures 16 and 17. The R_f of OPBI-SIPN (Figure 16b) is slightly higher than that for MPA-SIPN, that is explained by the higher difference between E_g and E_r . However, in both cases, $R_f > 95\%$ (Figure 16b); this indicates the good shape fixity performance. It can also be seen from Figure 16a that both SIPNs demonstrate reasonably fast recovery (recovery time of about 5–6 min), but in the case of OPBI-SIPN, the higher R_r value (97.9%) is achieved. It should be noted that

the previously described shape-memory polymers often demonstrate a higher recovery time (about 1–2 min).^[2] However, as mentioned earlier, in most cases such SMPs exhibit low reshaping temperatures (<100 °C), while T_{tran} of MPA-SIPN and OPBI-SIPN reach 119 and 155 °C, respectively, making them suitable for application in the high temperature shape memory fields. Moreover, as shown in this work, the PSCs from which our SIPNs were obtained, are suitable for the formation of 3D structures by the DLP method, that opens up broad prospects for 4D printing of functional shape-memory devices.

Figure 17a shows the transformation of 4D-printed blocks demonstrating the good shape-memory performance of both SIPNs. When the materials are heated above T_g (119 °C in the case of MPA-SIPN and 155 °C in the case of OPBI-SIPN), the blocks may be slightly bent by application of an external load to the central part of the samples. After cooling to room temperature, due to the large difference between E_g and E_r , the temporary shape is fixed. Upon the repeated heating of the samples above T_g , their original shape is successively restored.

A 4D-printed structure based on MPA-PSC in the form of a crocodile mouth can be used as a grip (Figure 17b). After raising

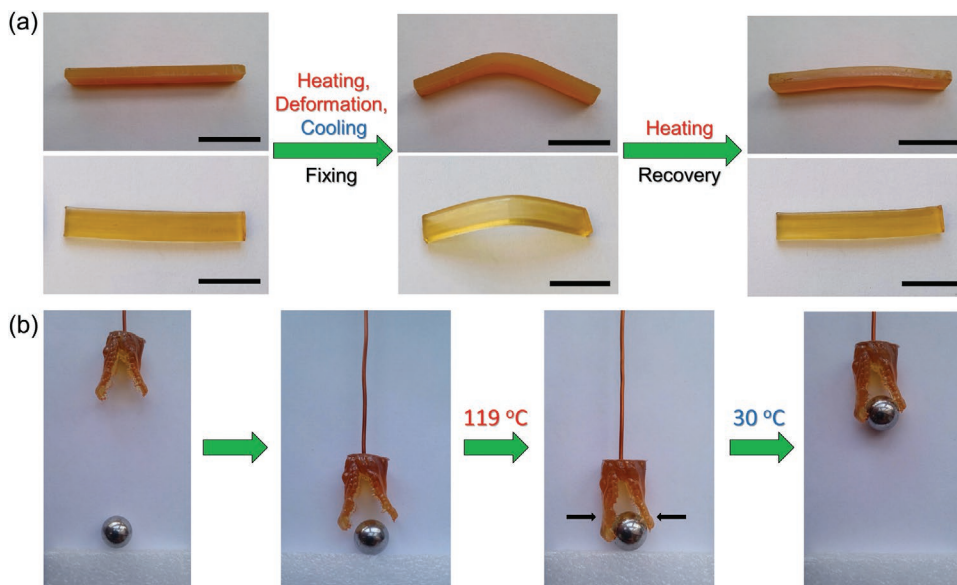


Figure 17. a) Shape-memory effect of DLP-based 4D-printed blocks based on OPBI-SIPN (top) and MPA-SIPN (bottom), scale bar is 1 cm. b) The 4D presentation of a printed gripper as a crocodile-shape.

the temperature to 119 °C and then cooling the structure down to 30 °C, the gripper can grip and hold a steel ball with a diameter of 10 mm, which weighs five times the mass of the gripper.

4. Conclusion

In summary, we report new photosensitive compositions based on high-performance poly(*N,N'*-(*m*-phenylene)isophthalamide) or poly(2,2'-(*p*-oxydiphenylene)-5,5'-dibenzimidazole), that can be used for DLP 4D printing of thermally stable semi-interpenetrating polymer networks. The method of post-processing (scCO₂-treatment, thermal treatment, or a combined technique) of the resulting semi-interpenetrating polymer networks strongly affects the mechanical properties of the materials. The 4D-printed structures possess excellent shape memory properties (R_f up to 98.7%, R_r up to 97.9% at $T_{tran} > 100$ °C) and can actively recover their original shape in a few minutes. Due to their high mechanical strength, thermal stability and good shape-memory performance, the obtained materials are promising for their potential application in advanced manufacturing, including aerospace and structural components industries.

Supporting Information

Supporting Information is available from the Wiley Online Library or from the author.

Acknowledgements

K.N.B., B.Ch.K., P.S.T., and V.F.B. contributed equally to this work. This study was financially supported by the RSF grant No. 20-73-00004 (preparation of photosensitive compositions based on OPBI), by the Ministry of Science and Higher Education within the framework of State Assignment to the Baikal Institute of Nature Management, Siberian Branch of the Russian Academy of Sciences (preparation of photosensitive compositions based on MPA) and within the framework of State Assignment to the FSRC «Crystallography and Photonics», Russian Academy of Sciences (additive technologies for DLP printing).

Conflict of Interest

The authors declare no conflict of interest.

Data Availability Statement

Research data are not shared.

Keywords

smart materials, shape-memory polymers, DLP 4D printing, semi-interpenetrating polymer networks, polybenzimidazole

Received: June 30, 2021
Revised: August 8, 2021
Published online:

- [1] A. A. Basheer, *Aircr. Eng. Aerosp. Technol.* **2020**, *92*, 1027.
- [2] A. Mitchell, U. Lafont, M. Holyřiska, C. Semprimoschnig, *Addit. Manuf.* **2018**, *24*, 606.
- [3] Z. Zhang, K. G. Demir, G. X. Gu, *Int. J. Smart Nano Mater.* **2019**, *10*, 205.
- [4] A. Bajpai, A. Baigent, S. Raghav, C. Ó. Brádaigh, V. Koutsos, N. Radacs, *Sustainability* **2020**, *12*, 10628.
- [5] L. Sun, W. M. Huang, Z. Ding, Y. Zhao, C. C. Wang, H. Purnawali, C. Tang, *Mater. Des.* **2012**, *33*, 577.
- [6] F. Momeni, S. Sabzpoushan, R. Valizadeh, M. R. Morad, X. Liu, J. Ni, *Renew. Energy* **2019**, *130*, 329.
- [7] S. Y. Hann, H. Cui, M. Nowicki, L. G. Zhang, *Addit. Manuf.* **2020**, *36*, 101567.
- [8] M. D. Hager, S. Bode, C. Weber, U. S. Schubert, *Prog. Polym. Sci.* **2015**, *49*, 3.
- [9] S. C. Ligon, R. Liska, J. Stampfl, M. Gurr, R. Muelhaupt, *Chem. Rev.* **2017**, *117*, 10212.
- [10] J. R. C. Dizon, A. H. Espera Jr., Q. Chen, R. C. Advincula, *Addit. Manuf.* **2018**, *20*, 44.
- [11] S. Mondal, *Mini-Rev. Org. Chem.* **2009**, *6*, 114.
- [12] T. Defize, R. Riva, J. M. Raquez, P. Dubois, C. Jérôme, M. Alexandre, *Macromol. Rapid Commun.* **2011**, *32*, 1264.
- [13] Q. Ge, X. Luo, E. D. Rodriguez, X. Zhang, P. T. Mather, M. L. Dunn, H. J. Qi, *J. Mech. Phys. Solids* **2012**, *60*, 67.
- [14] T. S. W. Keith Hearon, K. Gall, T. Ware, D. J. Maitland, J. P. Bearinger, *J. Appl. Polym. Sci.* **2010**, *116*, 144.
- [15] H. Luo, J. Hu, Y. Zhu, *Mater. Lett.* **2011**, *65*, 3583.
- [16] S. Ma, S. Wang, S. Jin, Y. Wang, J. Yao, X. Zhao, C. Chen, *Polymer (Guildf)* **2020**, *210*, 122972.
- [17] Z. Yang, Q. Wang, Y. Bai, T. Wang, *RSC Adv.* **2015**, *5*, 72971.
- [18] Z. Yang, F. Song, Q. Wang, T. Wang, *J. Polym. Sci., Part A: Polym. Chem.* **2016**, *54*, 3858.
- [19] X. Li, Y. Yang, Y. Zhang, T. Wang, Z. Yang, Q. Wang, X. Zhang, *Mater. Des.* **2020**, *191*, 108606.
- [20] Y. Shi, M. Yoonessi, R. A. Weiss, *Macromolecules* **2013**, *46*, 4160.
- [21] Z. Zhao, Y. Gu, D. Chao, X. Liu, *Eur. Polym. J.* **2019**, *116*, 336.
- [22] Q. Chen, L. Han, J. Ren, L. Rong, P. Cao, R. C. Advincula, *ACS Appl. Mater. Interfaces* **2020**, *12*, 50052.
- [23] J. M. García, F. C. García, F. Serna, J. L. de la Peña, *Prog. Polym. Sci.* **2010**, *35*, 623.
- [24] D. Aili, J. Yang, K. Jankova, D. Henkensmeier, Q. Li, *J. Mater. Chem. A* **2020**, *8*, 12854.
- [25] Q. Li, J. O. Jensen, R. F. Savinell, N. J. Bjerrum, *Prog. Polym. Sci.* **2009**, *34*, 449.
- [26] M. Hegde, V. Meenakshisundaram, N. Chartrain, S. Sekhar, D. Tafti, C. B. Williams, T. E. Long, *Adv. Mater.* **2017**, *29*, 1701240.
- [27] D. A. Rau, J. Herzberger, T. E. Long, C. B. Williams, *ACS Appl. Mater. Interfaces* **2018**, *10*, 34828.
- [28] J. Herzberger, V. Meenakshisundaram, C. B. Williams, T. E. Long, *ACS Macro Lett.* **2018**, *7*, 493.
- [29] Y. Guo, Z. Ji, Y. Zhang, X. Wang, F. Zhou, *J. Mater. Chem. A* **2017**, *5*, 16307.
- [30] D. S. Dudova, K. N. Bardakova, B. C. Kholkhoev, B. D. Ochirov, E. N. Gorenskaia, I. A. Farion, V. F. Burdukovskii, P. S. Timashev, N. V. Minaev, O. S. Kupriyanova, *J. Appl. Polym. Sci.* **2018**, *135*, 46463.
- [31] B. C. Kholkhoev, K. N. Bardakova, N. V. Minaev, O. S. Kupriyanova, E. N. Gorenskaia, T. M. Zharikova, P. S. Timashev, V. F. Burdukovskii, *Mendeleev Commun.* **2019**, *29*, 223.
- [32] P. J. Scott, D. A. Rau, J. Wen, M. Nguyen, C. R. Kasprzak, C. B. Williams, T. E. Long, *Addit. Manuf.* **2020**, *35*, 101393.
- [33] X. Kuang, K. Chen, C. K. Dunn, J. Wu, V. C. F. Li, H. J. Qi, *ACS Appl. Mater. Interfaces* **2018**, *10*, 7381.
- [34] P. J. Scott, V. Meenakshisundaram, M. Hegde, C. R. Kasprzak, C. R. Winkler, K. D. Feller, C. B. Williams, T. E. Long, *ACS Appl. Mater. Interfaces* **2020**, *12*, 10918.

- [35] D. V. Ganin, D. S. Dudova, B. S. Shavkuta, O. S. Korkunova, B. C. Kholkhoev, P. S. Timashev, V. F. Burdukovskii, N. V. Minaev, *Opt. Spectrosc.* **2020**, 128, 909.
- [36] G. Taormina, C. Sciancalepore, M. Messori, F. Bondioli, *J. Appl. Biomater. Funct. Mater.* **2018**, 16, 151.
- [37] M. Monzón, Z. Ortega, A. Hernández, R. Paz, F. Ortega, *Materials (Basel)* **2017**, 10, 64.
- [38] J. Bauer, A. G. Iazard, Y. Zhang, T. Baldacchini, L. Valdevit, *Opt. Express* **2020**, 28, 20362.
- [39] C. Quan, M. Soroush, M. C. Grady, J. E. Hansen, W. J. Simonsick, *Macromolecules* **2005**, 38, 7619.
- [40] B. Steyrer, P. Neubauer, R. Liska, J. Stampfl, *Materials (Basel)* **2017**, 10, 1445.
- [41] C. Coon, B. Pretzel, T. Lomax, M. Strlič, *Heritage Sci.* **2016**, 4, 1.
- [42] J. Z. Manapat, J. D. Mangadlao, B. D. B. Tiu, G. C. Tritchler, R. C. Advincula, *ACS Appl. Mater. Interfaces* **2017**, 9, 10085.
- [43] D. Wu, Z. Zhao, Q. Zhang, H. J. Qi, D. Fang, *Soft Matter* **2019**, 15, 6151.
- [44] J. C. Moller, R. J. Berry, H. A. Foster, *Polymers (Basel)* **2020**, 12, 466.
- [45] D. Karalekas, A. Aggelopoulos, *J. Mater. Process. Technol.* **2003**, 136, 146.
- [46] L. J. White, V. Hutter, H. Tai, S. M. Howdle, K. M. Shakesheff, *Acta Biomater.* **2012**, 8, 61.
- [47] X. Guo, H. Ni, M. Li, L. Zhang, Y. Wang, L. Ding, *Indian Geotech. J.* **2018**, 48, 384.
- [48] A. I. Cooper, *J. Mater. Chem.* **2000**, 10, 207.
- [49] A. R. C. Duarte, J. F. Mano, R. L. Reis, *Int. Mater. Rev.* **2009**, 54, 214.
- [50] J. L. Kendall, D. A. Canelas, J. L. Young, J. M. DeSimone, *Chem. Rev.* **1999**, 99, 543.
- [51] Y. S. Bharathi, M. M. Reddy, G. R. Reddy, S. V. Naidu, *Polymer (Guildf)* **2010**, 5, 95.
- [52] A. Y. Leykin, A. I. Fomenkov, E. G. Galpern, I. V. Stankevich, A. L. Rusanov, *Polymer (Guildf)* **2010**, 51, 4053.
- [53] S. Zhang, Q. Ran, Q. Fu, Y. Gu, *Macromolecules* **2018**, 51, 6561.
- [54] J. Bennett, *Addit. Manuf.* **2017**, 18, 203.
- [55] S.-J. Kwon, Y.-J. Park, S.-H. Jun, J.-S. Ahn, I.-B. Lee, B.-H. Cho, H.-H. Son, D.-G. Seo, *Restor. Dent. Endod.* **2013**, 38, 105.
- [56] S. Koo, S. M. Santoni, B. Z. Gao, *J. Mater. Res.* **2017**, 32, 128.
- [57] J. T. Cabral, S. D. Hudson, C. Harrison, J. F. Douglas, *Langmuir* **2004**, 20, 10020.
- [58] A. Vitale, M. G. Hennessy, O. K. Matar, T. Cabral, *Macromolecules* **2015**, 48, 198.
- [59] J.-P. Fouassier, J. F. Rabek, *Radiation curing in polymer science and technology: Practical aspects and applications*, Springer Science & Business Media, Berlin, Germany **1993**.
- [60] C. Kolb, N. Lindemann, H. Wolter, G. SEXTL, *J. Appl. Polym. Sci.* **2021**, 138, 49691.
- [61] A. D. Benjamin, R. Abbasi, M. Owens, R. J. Olsen, D. J. Walsh, T. B. Lefevre, J. N. Wilking, *Biomed. Phys. Eng. Express* **2019**, 5, 025035.
- [62] H. Quan, T. Zhang, H. Xu, S. Luo, J. Nie, X. Zhu, *Bioact. Mater.* **2020**, 5, 110.
- [63] B. Zou, X. Fu, B. Zou, H. Xing, L. Li, Y. Li, X. Wang, *Ceram. Int.* **2019**, 45, 17630.
- [64] B. Díaz-Reinoso, A. Moure, H. Domínguez, J. C. Parajó, *J. Agric. Food Chem.* **2006**, 54, 2441.
- [65] D. Lascano, L. Quiles-carrillo, S. Torres-giner, T. Boronat, N. Montanes, *Polymers (Basel)* **2019**, 11, 1354.
- [66] D. Ratna, J. Karger-Kocsis, *Polymer (Guildf)* **2011**, 52, 1063.